Check for updates

PHYSICAL SCIENCES

3D active-matrix multimodal sensor arrays for independent detection of pressure and temperature

Youngmin Jo[1]†, Youngoh Lee[2], Jimin Kwon[3], Seongju Kim[4], Gyungin Ryu[4], Soyoung Yun[4], Sanghoon Baek[4]*‡, Hyunhyub Ko[2]*, Sungjune Jung[1,4]*

Copyright © 2025 The Authors, some rights reserved; exclusive licensee American Association for the Advancement of Science. No claim to original U.S. Government Works. Distributed under a Creative Commons Attribution NonCommercial License 4.0 (CC BY-NC).

Pressure and temperature sensing simultaneously and independently is crucial for creating electronic skin that replicates complex sensory functions of human skin. Thin-film transistor (TFT) arrays with sensors have enabled cross-talk–free spatial sensing. However, the thermal dependence of charge transport in semiconductors has resulted in interference between thermal and pressure stimuli. We develop multimodal sensor arrays based on three-dimensional integration of an active matrix to detect temperature and pressure independently. Our approach includes a calibrated compensation to decouple temperature and pressure signals. An individual pixel device consists of a TFT-based pressure sensor layered above a TFT-based temperature sensor. The detected temperature is used to compensate for the thermal effect on TFT-based pressure sensors. We develop large-area sensor arrays to enable accurate detection of two-dimensional pressure and temperature, leveraging these technologies to demonstrate advanced robotic grippers. The grippers stably grasp and lift a cup regardless of temperature, proving their possibility in skin-like electronic applications.

INTRODUCTION

The cutaneous sensation of mechanical and thermal stimuli is essential for perceiving and interacting with the world (*1*). Taking inspiration from the vital function of human skin, flexible sensors have been extensively investigated to detect external multistimuli in various environments, including nonflat surfaces and shape-changing objects (*2*–*5*). Because of their wide applicability, they have shown great potential in electronic skin applications such as health care monitoring, prostheses, and robotics (*6*–*10*). Mimicking the complex sensory system of human skin, flexible multimodal sensors that can detect multiple stimuli have also emerged to provide more comprehensive and valuable information (*11*–*13*). Their multimodality was achieved either by the integration of independent sensors or the utilization of multistimuli responsive materials (*14*, *15*).

In multimodal sensors, it is essential to distinguish signals in the presence of multiple stimuli to ensure an accurate and undistorted output (*16*). Attempts have been made to minimize such interference issues. Various strategies have been suggested depending on the multi-sensing mechanism, including calibrated compensation, integrating sensing units with high selectivity, intrinsically decoupled sensing parameters, and different response times (*17*–*24*). To advance multimodal sensors as more practical alternatives to real skin, it is highly desirable for the sensors to detect multiple tactile stimuli over a large area, even spatially. However, this signal discrimination is usually limited to a single device. Most multimodal sensor arrays are based on passive-matrix architectures, which are vulnerable to cross-talk between pixels. A signal transmitted to one pixel device still unintentionally affects other pixel devices.

Adopting thin-film transistors (TFTs) as switching components in a pixel device has attracted enormous attention for high-performance two-dimensional (2D) detection of stimuli. Originating in the display industry (*25*), active-matrix architectures based on TFTs offer distinct advantages such as low power consumption and minimal crosstalk (*26*–*33*). To achieve a reliable performance of the active-matrix sensor arrays, it is crucial that the electrical current of the TFTs remains unaffected by the variation of nontarget stimuli. For example, in the pressure-sensing active-matrix sensor, TFTs are required to be insensitive to temperature fluctuations. However, TFTs, regardless of semiconductor materials and types used, generally display temperature-dependent charge transport behaviors, which can be elucidated by various models, such as band-like transport, multiple trap and release, variable range hopping, and charged-impurity scattering (*34*–*37*). As a result, because of the intrinsic properties of transistors, most active matrix sensing arrays experience signal distortion when exposed to temperature variations, limiting their effectiveness and demonstrations in room temperature environments (*38*, *39*). Here, we introduce for the first time the monolithic and 3D transistor-on-transistor active-matrix structure to develop 3D-integrated multimodal sensor arrays for detecting pressure and temperature with stimulus discriminability. For the multimodal sensing in a single pixel, we monolithically integrate a TFT array on top of another array to form 3D stacked active-matrix arrays. On the top TFT array, a large-area piezoresistive sheet is integrated to achieve a TFT-based pressure sensor array operating between 0 and 20 kPa. The intrinsic temperature dependence of the semiconductor in bottom TFTs is exploited to detect temperatures between 25° and 50°C. The monolithic 3D integration of the TFTs enables temperature measurement that can correct distortions in the pressure signal caused by the intrinsic thermal response of semiconductors or the integrated piezoresistive sheet. To eliminate the undesirable thermal effects, we develop a calibrated compensation

[1]Department of Convergence IT Engineering, Pohang University of Science and Technology, 77 Cheongam-Ro, Pohang 37673, Republic of Korea. [2]School of Energy and Chemical Engineering, Ulsan National Institute of Science and Technology, Ulsan 44919, Republic of Korea. [3]Department of Electrical Engineering, Ulsan National Institute of Science and Technology, Ulsan 44919, Republic of Korea. [4]Department of Materials Science and Engineering, Pohang University of Science and Technology, 77 Cheongam-Ro, Pohang 37673, Republic of Korea.
*Corresponding author. Email: sh313.baek@samsung.com (S.B.); hyunhko@unist.ac.kr (H.K.); sjjung@postech.ac.kr (S.J.)
†Present address: Thin Film Materials Research Center, Korea Research Institute of Chemical Technology (KRICT), 114, Gajeong-ro, Yuseong-gu, Daejeon 34114, Republic of Korea.
‡Present address: Semiconductor R&D Center, Samsung Electronics, 1 Samsungjeonja-Ro, Hwaseong 18488, Republic of Korea.

Downloaded from https://www.science.org at Ulsan National Institute of Science and Technology on February 04, 2025

method by using the linear temperature sensitivity of the measured temperature information. With the compensation, the multimodal 3D sensor arrays achieve accurate mappings of pressure and temperature independently. Last, a robotic gripper with the 3D sensor array is demonstrated to successfully grasp and lift both room temperature and hot cups. The developed device suggests a new direction for the next-generation skin-like electronics through 3D integration of multiple active-matrix sensors.

RESULTS

Design and fabrication of the multimodal 3D sensor array

The multimodal 3D sensor array consists of a large-area piezoresistive sheet and two monolithically stacked active-matrix layers fabricated on an ultrathin film (Fig. 1, A and B). Each pixel device in the multimodal 3D sensor has a vertical configuration of a one-transistor–one-resistor (1T-1R) pressure (*P*) sensor on top of a one-transistor temperature (*T*) sensor (Fig. 1C). Figure 1D presents the circuit representation of the 3D sensor pixel device, where the drain currents of the bottom and top TFTs are modulated by temperature and pressure, respectively. For the array demonstration, each drain electrode was connected to its corresponding bit line, while the source electrodes were connected to the ground. The gate electrode was shared between the top and bottom devices, allowing for data reading in the matrix with only a single word line. The electric current of the 3D sensors is used as a variable to quantify the stimulus intensity. The detection of pressure is enabled by a piezoresistive sheet with interlocked microdome structures (Fig. 1E). When a pressure load is applied, the interlocked microstructure of the piezoresistive sheets deforms. The deformation decreases the resistance of the sheet, which, in turn, increases the current of the 1T-1R pressure sensor (*40*, *41*). Without additional components, the bottom transistors are used as pressure-insensitive temperature sensors by exploiting the intrinsic temperature dependence of the organic semiconductor. For temperature sensing, poly[2,5-(2-octyldodecyl)-3,6-diketopyrrolopyrrole-alt-5,5-(2,5-di(thien-2-yl)thieno [3,2-b]thiophene)] (DPP-DTT) was used as a conjugated polymer channel layer of the bottom TFTs, which exhibited temperature-dependent charge transport (*42*). However, this intrinsic characteristic causes undesirable temperature-dependent output signals from the top pressure sensors. This issue typically occurs with TFT-based sensors, where the charge transport behavior of either semiconductors or integrated sensing components is thermally dependent. To eliminate these undesired effects on the top TFT-based pressure sensor, we use a calibrated compensation method that uses the vertically aligned configuration of TFTs (Fig. 1F). This method compensates for the electric current (I_P) of the pressure sensor by using the temperature information derived from the electric current of the temperature sensor directly below the pressure sensor, regardless of temperature. Therefore, the multimodal 3D sensors provide temperature-independent output signals, which enable simultaneous and independent detection of pressure and temperature.

The monolithic 3D integration of TFTs is key to simultaneous multistimuli detection. To realize the multimodal 3D sensors, the

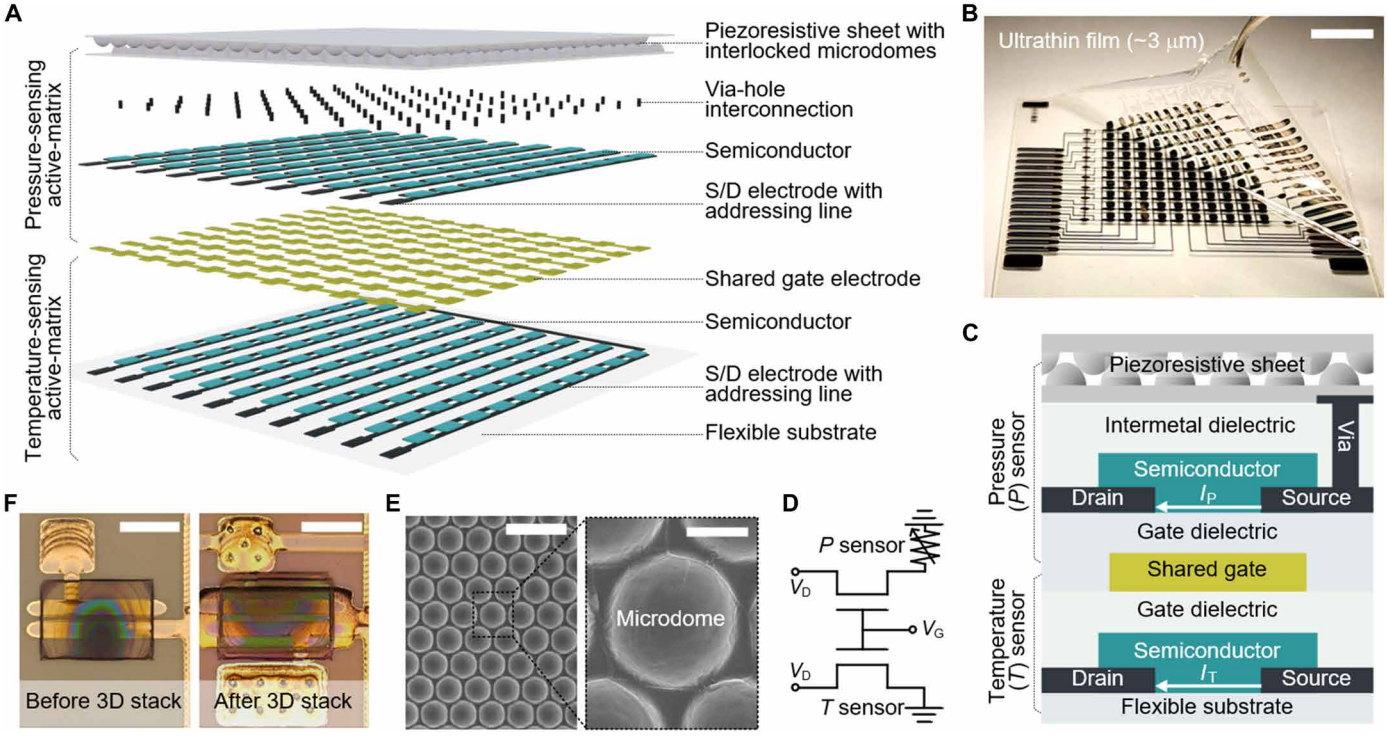

Fig. 1. Design of the multimodal 3D sensor arrays. (**A**) 3D schematic of the 10-by-10 multimodal 3D sensor array consisting of a pressure-sensing active-matrix and a temperature-sensing active-matrix. (**B**) Photograph of the 10-by-10 3D stacked active-matrix fabricated on an ultrathin substrate. Scale bar, 1 cm. (**C**) Schematic cross-sectional view and (**D**) circuit of the multimodal 3D sensor. (**E**) Scanning electron microscopy images of rGO/PVDF microdome structures. Scale bar, 25 μm. Inset: A single microdome structure. Scale bar, 5 μm. (**F**) Optical microscopy images of the semiconductor areas before (left) and after (right) the 3D stacking process. Scale bar, 800 μm.

Downloaded from https://www.science.org at Ulsan National Institute of Science and Technology on February 04, 2025

fabrication process of 3D stacked TFTs was assisted by sophisticated printing design rules. Furthermore, the entire process was conducted under 120°C to minimize thermal damage to the bottom TFT. First, the source and drain (S/D) electrodes were inkjet-printed on a parylene-coated glass substrate, and a p-type organic semiconductor ink was patterned using a pneumatic nozzle printer. Here, a conjugated polymer semiconductor was used for temperature sensing without any additional components, such as thermistors, which simplified the fabrication process of TFT-based temperature sensors. Next, a parylene gate dielectric layer was deposited due to its high resistance to organic solvents. The gate electrodes were then inkjet-printed. The gate electrodes were used to control both top and bottom TFTs. The common-gate structure led to fewer fabrication processes and a simpler interconnect design. After the completion of the bottom TFT, the top TFT was continuously fabricated on top of the bottom device. A parylene intermetal dielectric layer was deposited on the 3D stacked TFTs, and via-holes were created at each pixel using nanosecond pulsed laser ablation (fig. S1). The via-holes were subsequently filled through inkjet printing to extend the source electrodes of the top device to the air. The extended electrodes were connected to the piezoresistive sensor sheet. The piezoresistive sheet was fabricated by stacking two layers of reduced graphene oxide/polyvinylidene difluoride (rGO/PVDF) composite microdome arrays. The GO/PVDF solution was prepared by introducing GO into the PVDF matrix. The composite solution was poured on a micro-patterned mold and reduced to rGO/PVDF with microdome structures. Because of the simplicity and scalability of the fabrication process, the size of piezoresistive sheets could be customized, which enabled the integration of the sensor sheet on the large-area 3D stacked TFT arrays. The detailed fabrication process is described in fig. S2.

Electrical characterization of the multimodal 3D sensors

We characterized the 3D stacked TFTs, including the top TFT-based pressure sensors and the bottom TFT-based temperature sensors. Transfer characteristics ($|I_D|$ versus V_{GS}) of TFTs were measured in a saturation regime with $V_{DS} = -10$ V. Notably, the bottom TFTs showed similar electrical performance before and after stacking the top TFTs (Fig. 2A). Twenty-five pairs of the top and bottom TFTs exhibited typical transfer characteristics with 100% yield (Fig. 2B) and high uniformity (Fig. 2, C to E). The average carrier mobility (μ) of the top and bottom TFTs were 0.09 ± 0.02 and 0.09 ± 0.01 $cm^2 V^{-1} s^{-1}$, respectively (Fig. 2C). The average threshold (V_{TH}) was -0.99 ± 0.16 (top) and -1.12 ± 0.15 V (bottom) (Fig. 2D). The average subthreshold slope (*SS*) was 405 ± 52 (top) and 352 ± 44 mV/dec (bottom) (Fig. 2E). Moreover, the stacked TFTs showed negligible degradation of electrical performance under a bending radius of 10 mm (fig. S3).

For pressure sensing, the 3D stacked TFTs were integrated with the rGO/PVDF piezoresistive sheets that served as a pressure-sensitive resistor of the 1T-1R pressure sensor. After the integration, the I_P was measured to show the transfer characteristics under various pressure loads ranging from 0 to 20 kPa at 25°C (Fig. 2F). The $|I_P|$-V_{GS} curves showed upward shifts with increasing pressure loads that increased the contact area of the microdomes in the piezoresistive sheets and hence their conductivity. The electrical properties of the sheets and the top TFTs were characterized under the same stimulus conditions used for the pressure sensors (Fig. 2G). It can be seen that the increase of I_P was mainly from the piezoresistive sheets, where the drain current of the TFT was constant, while the resistance of the sheets decreased with increasing pressure. As a result, the 1T-1R sensor detected pressure changes between 0 and 20 kPa. Subsequently, the pressure calibration curve (relative I_P versus applied pressure) was plotted at $V_{GS} = V_{DS} = -10$ V (Fig. 2H). The relative value was defined as $|I_P/I_{P0}|$, where the I_{P0} was the drain current measured at 0 kPa and 25°C. The pressure-sensitivity $[(\Delta I_P/I_{P0})/\Delta P]$ of the device was nonlinear. The nonlinear pressure sensitivity resulted from the interlocked microstructures, where the contact area changed more significantly at lower pressures before saturating due to deformation limits (*43*). To accurately correlate drain current values with the corresponding pressure values, the pressure range (0 to 20 kPa) was divided into three linear segments (0 to 1 kPa, 1 to 6 kPa, and 6 to 20 kPa). The three segments exhibited pressure sensitivities of 2.64, 0.22, and 0.02 kPa^{-1}, respectively. The pressure sensor exhibited negligible hysteresis during pressure loading and unloading. In addition, the device showed a reliable real-time response to the applied pressures and reasonable device-to-device variation with a relative SD (RSD) of less than 15% (Fig. 2I and fig. S4A).

To validate feasibility as a temperature sensor, the transfer characteristics of the bottom TFTs were measured between 25° and 50°C. (Fig. 2J). The temperature range was determined on the basis of the permissible and nonhazardous range of human skin, which is not perceived as nociceptive (*44*, *45*). The drain current increased with increasing temperature. The temperature dependence was analyzed by extracting the mobility and threshold voltage (Fig. 2K). When the temperature increased from 25° to 50°C, the mobility increased by 49%, while the threshold decreased by 37%. The increase in mobility and decrease in threshold can be rationalized by thermally activated charge transport in conjugated polymers (*46*) and thermally induced transition from deep traps to shallow traps, respectively (*47*). The relative current values of the temperature sensor were defined as $|I_T/I_{T0}|$, where the I_{T0} was the drain current measured at 25°C and 0 kPa. The temperature sensor showed a linear sensitivity with insignificant hysteresis (Fig. 2L). The $|I_T/I_{T0}|$ increased by 68% from 25° to 50°C, corresponding to the temperature coefficient of resistance of -2.72% $°C^{-1}$, which exceeded previously reported values (*48*–*52*). Furthermore, the temperature sensor detected a wide range of temperatures in real time and showed uniform sensitivity with an RSD of less than 10% (Fig. 2M and fig. S4B).

Calibrated compensation for the detection of pressure independent of temperature

We examined the cross-sensitivity of the bottom temperature sensors and the top pressure sensors. The drain current of the temperature sensors was measured between 0 and 20 kPa, while the pressure sensors were investigated between 25° and 50°C. Although the temperature sensors were immune to pressure changes due to sufficiently rigid thin-film layers (fig. S5), the pressure sensors exhibited unintended temperature dependence. As shown in Fig. 3A, the I_P/I_{P0} versus P curves of the pressure sensors showed an upward shift along with the increased temperature, which distorted pressure values derived from the measured I_P. This unwanted shift was supported by the temperature-dependent charge transport in both the top TFTs and the piezoresistive sheets (fig. S6). To minimize the thermally induced fluctuations, we proposed a calibrated compensation method that converted the I_P values at any T, $I_{P(T)}$, into the I_P values at a reference temperature (T_0).

Downloaded from https://www.science.org at Ulsan National Institute of Science and Technology on February 04, 2025

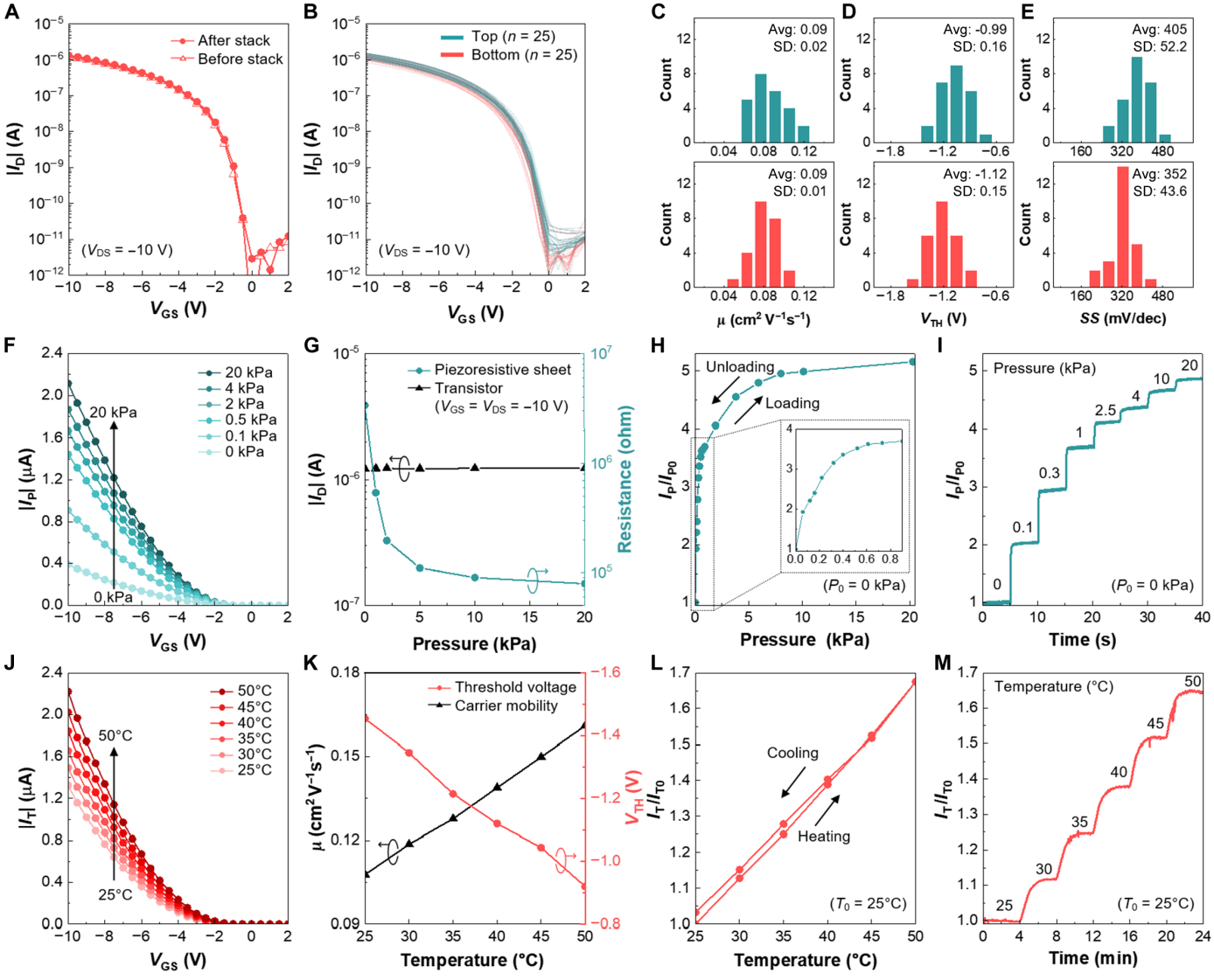

Fig. 2. Electrical characterization of the multimodal 3D sensors. (**A**) Representative transfer characteristics of the bottom TFT before and after the fabrication process for the top TFT. (**B**) Transfer characteristics of 25 pairs of bottom and top TFTs. Histograms of (**C**) carrier mobility (μ), (**D**) threshold voltages (V_{TH}), and (**E**) subthreshold slope (*SS*) extracted from the transfer characteristics (n = 25). (**F**) Transfer characteristics of the top TFT-based pressure sensor with increasing pressures from 0 to 20 kPa. (**G**) Drain current (I_P) of the top TFT and resistance of the piezoresistive sheets as a function of applied pressure. (**H**) Relative current (I_P/I_{P0}) as a function of applied pressure during loading and unloading cycles. Inset: Magnified I_P/I_{P0}-P curve between 0 and 0.9 kPa. (**I**) Real-time response of the pressure sensor to gradually increasing pressure loads from 0 to 20 kPa. (**J**) Transfer characteristics of the bottom TFT-based temperature sensor with increasing temperatures from 25° to 50°C. (**K**) Carrier mobility and a threshold voltage of the bottom TFT as a function of ambient temperature. (**L**) Relative current (I_T/I_{T0}) as a function of ambient temperature during heating and cooling cycles. (**M**) Real-time response of the temperature sensor to gradually increasing temperature from 25° to 50°C.

The main idea for the compensation method is based on the linear thermal response of the pressure sensors (Fig. 3B), although the pressure sensitivity is nonlinear. First, the relationships between I_P/I_{P0} and T were plotted under various temperatures from 25° to 50°C. The temperature sensitivity of the pressure sensors (S_P) was defined as a slope determined after linear regression of each I_P/I_{P0} versus T curve. Notably, the thermal response of the pressure sensors exhibited a linear relationship with nearly the same slope across different pressure values. The average of R^2 (coefficient of determination) value for each curve was 0.9986, and the RSD of the sensitivity was only 3%. In other words, the sensitivity was linear and similar regardless of pressure. The linear dependence on temperature can be attributed to the linear thermal response of the top TFT (fig. S6A) and the conductance of the integrated piezoresistive sheet (fig. S6B). By exploiting the linear and uniform sensitivity, the calibrated compensation was developed. The compensation process consists of two steps (fig. S7). First, it is necessary to calculate the temperature difference (ΔT^*) between the unknown temperature (T^*) and the T_0. The pressure-independent temperature sensitivity (S_T) of the temperature sensor is defined as $(I_{T2} - I_{T1})/(T_2 - T_1)$, where T_1 and T_2 are arbitrary temperature values between 25° and 50°C. After substituting T_0 and T^* for T_1 and T_2, respectively, the following equation is established

Downloaded from https://www.science.org at Ulsan National Institute of Science and Technology on February 04, 2025

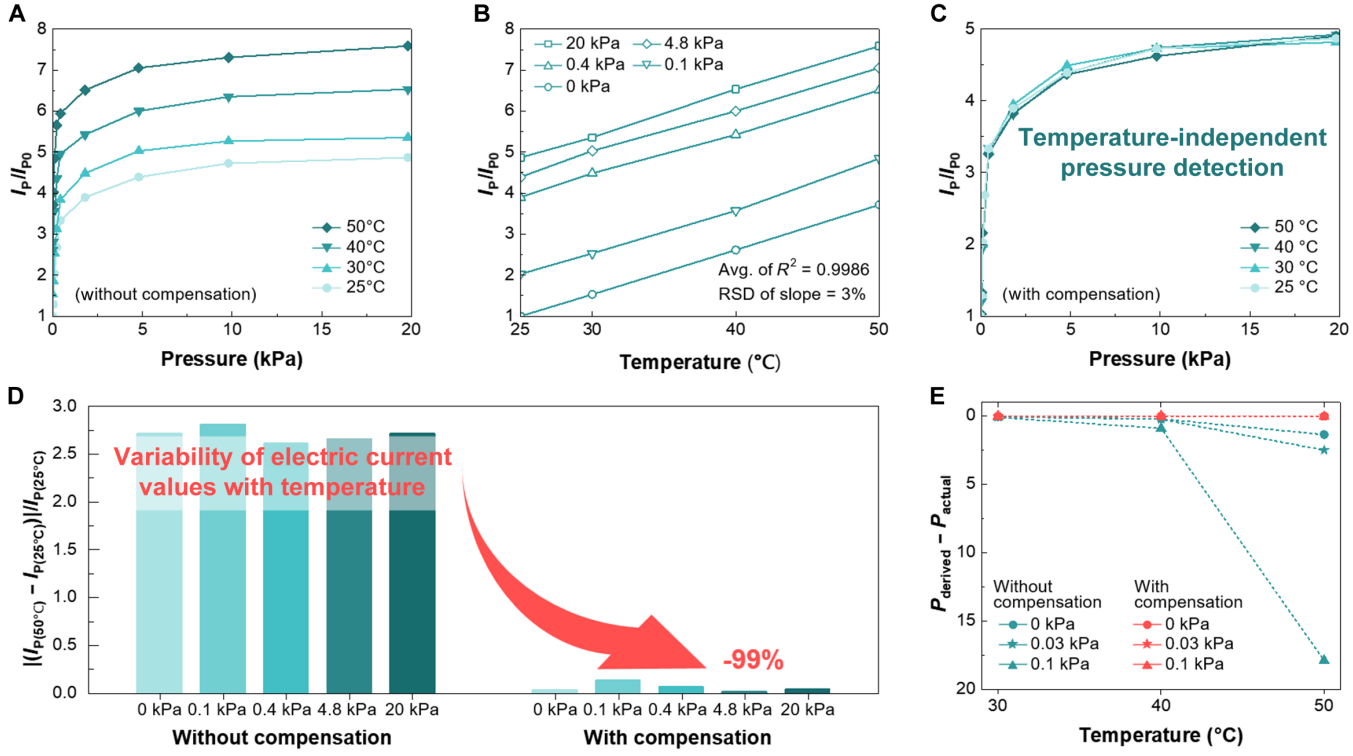

Fig. 3. Calibrated compensation for temperature-independent detection of pressure. (**A**) Relative current of the top pressure sensor as a function of applied pressure with various temperatures. (**B**) Relative current of the top pressure sensor as a function of ambient temperature at various pressures. (**C**) Relative current of the top pressure sensor as a function of applied pressure at various temperatures after calibrated compensation. (**D**) Variability of I_P values with temperature between 25° and 50°C. (**E**) Differences between derived and actual pressure values as a function of temperature. Turquoise green symbols represent results without compensation, and coral red symbols represent results with compensation. RSD, relative SD.

$$\Delta T^* = \left(T^* - T_0\right) = S_T / \left(I_{T^*} - I_{T0}\right) \quad (1)$$

Because the S_T and I_{T0} are predetermined by measuring I_T at two known temperatures, including T_0, the ΔT^* is easily calculated after measuring the I_{T^*}. Next, the ΔT^* is used to convert the $I_{P(T)}$ to $I_{P(T0)}$. Because of the linear and uniform S_P, the $I_{P(T0)}$ can be formulated by

$$I_{P(T0)} = I_{P(T)} - S_P \times \Delta T^* \quad (2)$$

The above equation shows that any measured $I_{P(T)}$ is converted to the temperature-independent $I_{P(T0)}$ by subtracting the thermal distortion term ($S_P \times \Delta T^*$). The suggested thermal compensation was effective across all pressure ranges, as S_P was nearly identical regardless of the pressure values.

To verify the compensation method, we converted all data in the three $I_{P(T)}/I_{P0}$ versus P curves at 30°, 40°, and 50°C to $I_{P(T0)}$ with the T_0 of 25°C (Fig. 3C). After the conversion, the four relationship curves overlapped and appeared as a single curve, which could facilitate the extraction of temperature-independent pressure values over a wide temperature range. The effectiveness of the compensation was also evaluated quantitatively. The variability of $I_{P(T)}$ with temperature was estimated as $|I_{P(50°C)} - I_{P(25°C)}|/I_{P(25°C)}$ (Fig. 3D). With the implementation of the compensation method, the average of the variability values decreased by 99% despite the considerable variability caused by temperature differences of 25°C without this compensation. The marked reduction in variability significantly enhanced the accuracy of the pressure sensor. To quantify this improvement, we defined temperature-induced errors as the differences between the actual and derived pressure values. The errors were calculated using measured $I_{P(T)}$ values based on the $I_{P(25°C)}$ versus P relationship and plotted as a function of the measurement temperature (Fig. 3E). Without compensation, the errors increased with both rising temperature and pressure, meaning that higher temperatures and pressures led to greater distortion. For example, at 50°C, a pressure of 0.1 kPa was erroneously perceived as 17.9 kPa, whereas 0 kPa was perceived as 1.4 kPa. The unexpected influence of pressure on the errors was elucidated by analyzing the slope of the $I_{P(T)}$-P curve at higher pressures, the slope became steep (Fig. 2H). A less steep slope results in a greater horizontal shift for a given vertical change, exacerbating the error as temperature rises. However, with the compensation method in place, temperature-induced errors became negligible across all temperatures and pressures, demonstrating that the method effectively mitigated these mismeasurements.

Spatial measurement of pressure and temperature

We developed a 10-by-10 multimodal 3D sensor array using a 3D active-matrix technology, which enabled real-time mapping of both pressure and temperature. The innovative active-matrix with transistor-on-transistor architecture facilitated the simultaneous measurement of these parameters. To demonstrate its capability, we placed two objects of identical weight but differing temperatures (25° and 50°C) on the sensor array (Fig. 4A). The hot object introduced both mechanical and thermal stimuli to the multimodal 3D sensor arrays. Measurement was

Downloaded from https://www.science.org at Ulsan National Institute of Science and Technology on February 04, 2025

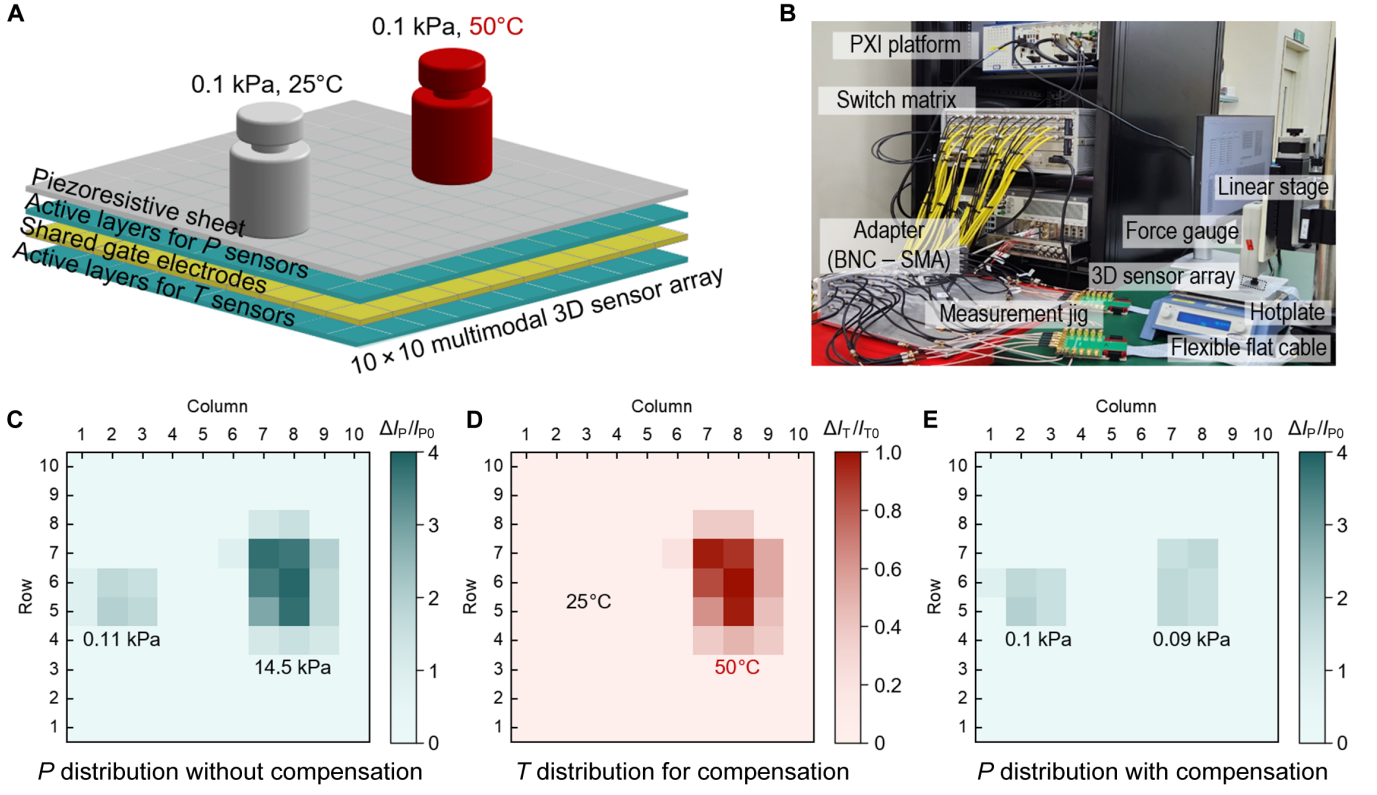

Fig. 4. The multimodal 3D sensor array for spatial measurement. (**A**) 3D schematic of the 10-by-10 multimodal 3D sensor array with two objects of equal weight but different temperatures (25° and 50°C). Inset: Magnified 3D schematic showing deformation and heat transfer induced by the hot object. (**B**) A photograph of the custom-built array measurement system based on the National Instruments PXI platform and switch matrix. (**C**) Heatmap of relative current change measured from the pressure-sensing active matrix without compensation. (**D**) Heatmap of relative current change measured from the temperature-sensing active matrix for the calibrated compensation. (**E**) Heatmap of relative current change measured from the pressure-sensing active matrix with the compensation. BNC–SMA, Bayonet Neill–Concelman to SubMiniature version A.

performed in real time using a custom-built automated *I-V* measurement system, which was based on the National Instruments (NI) PXI platform with a switch matrix (Fig. 4B). The voltage signals generated from the PXI platform were transmitted to a pixel device through the switch matrix, data transmission line, and measurement fixture. The PXI platform also measured the drain current of the pixel device. The current-voltage relation (*I-V*) measurement was repeated until the drain current of all pixel devices was measured in sequence. The measurement system was controlled by automation software developed in the NI LabVIEW environment. Detailed information on the automation system is described in fig. S8.

The I_P values of each pixel were measured across the matrix to derive the pressure. It was assumed that the pixel displaying the maximum pressure value indicated the point of most definitive contact between the object and the sensor. The maximum values of the 2D pressure profiles under the room temperature and hot object were 0.11 and 14.5 kPa, respectively (Fig. 4C). This discrepancy was due to the temperature-induced errors previously mentioned. To acquire accurate pressure information regardless of the temperature, we used the 3D sensor array integrated with the proposed compensation method. First, the bottom active-matrix sensor detected the 2D temperature distribution (Fig. 4D), where the maximum temperature measured corresponded precisely to the actual temperature of each object. Second, we adjusted the I_P values from the top active-matrix sensor using the acquired 2D temperature data (Fig. 4E). After applying the compensation, the maximum pressures recorded under the room temperature and hot object were 0.1 and 0.09 kPa, respectively, reducing the pressure disparity by 99.93% compared to the uncompensated results. Consequently, the 3D sensor array, enhanced with the calibrated compensation, successfully provided accurate spatial temperature mapping and 2D pressure distribution.

Smart robotic gripper application

To effectively harness accurate real-time temperature and pressure information, we implemented a closed-loop control system for a robotic gripper designed to grasp and lift a cup filled with either room temperature or hot (50°C) water as shown in Fig. 5A. The gripper was equipped with a multimodal 3D sensor array affixed to one of its fingers (inset in Fig. 5A). A specific 5-by-3 section of the matrix served as the sensing area, providing real-time feedback through a connection to a custom-built control system (fig. S9). The operation protocol was as follows (Fig. 5B). First, the gripper was initialized, and the I_T and I_P values from each pixel within the sensing area were collected at a frequency of 9 Hz. The spatial I_T data facilitated the correction of the distorted I_P values. The corrected spatial I_P values were averaged and compared with a predetermined threshold. This threshold, which was set to prevent breakage or slippage of the cup

Downloaded from https://www.science.org at Ulsan National Institute of Science and Technology on February 04, 2025

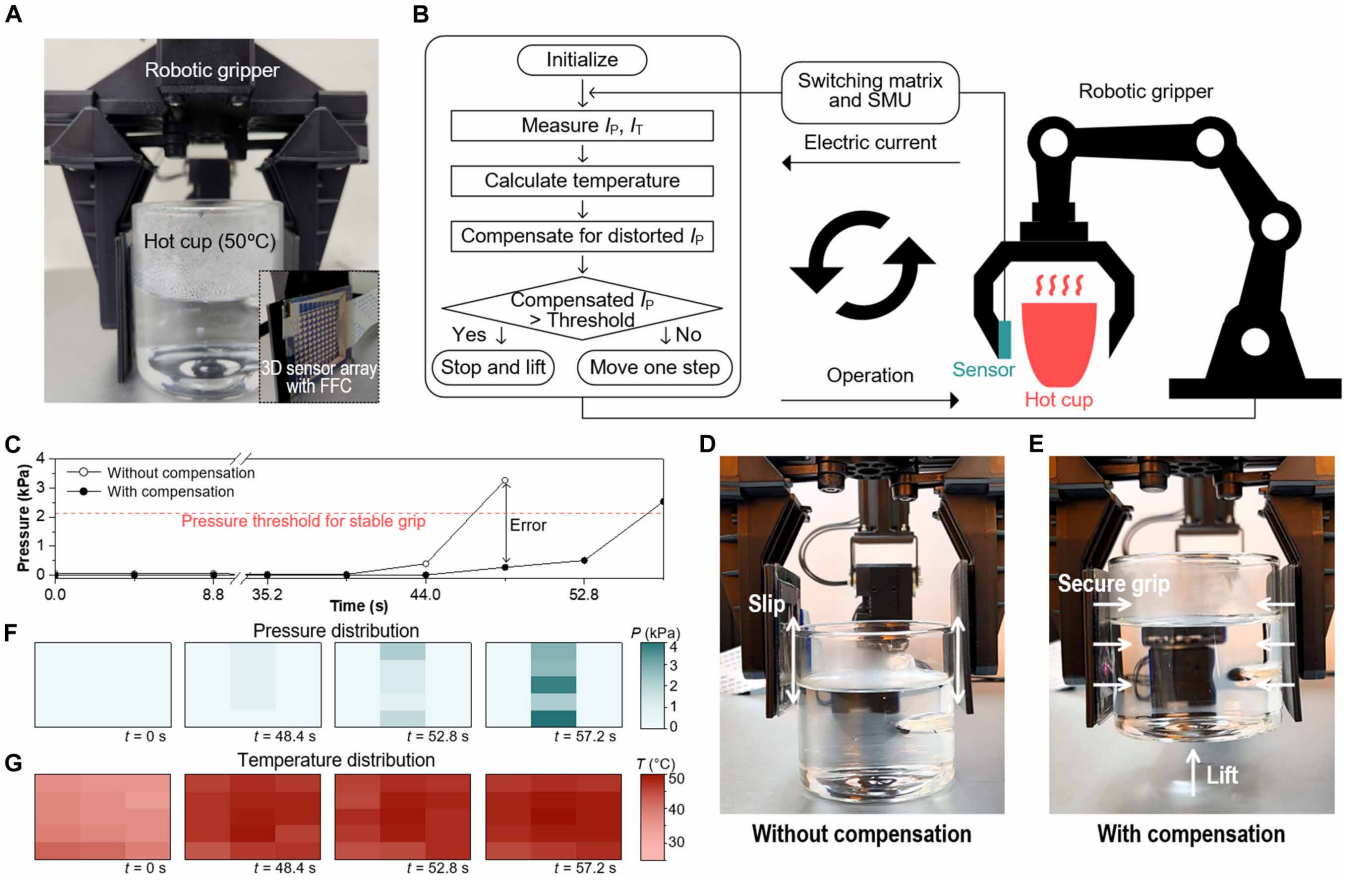

Fig. 5. Application to the robotic gripper. (**A**) Photograph of a cup containing hot water and the robotic gripper equipped with the multimodal 3D sensor array. Inset: Rear view of the multimodal 3D sensor array connected to a flexible flat cable (FFC) for the robotic demonstration. (**B**) Schematic diagram of the robotic gripper controlled by the feedback system. (**C**) Real-time pressure data measured from the multimodal sensor array without and with compensation. Snapshots of the gripper (**D**) failing and (**E**) successfully lifting the hot cup. Spatiotemporal readings of (**F**) pressure and (**G**) temperature measured from the multimodal sensor array with calibrated compensation.

(~2 kPa), proved effective for securely grasping and lifting a cup at room temperature (fig. S10 and movie S1). If the average I_P value fell below this threshold, then the gripper's fingers incrementally approached the cup, with drain currents measured at each movement. Conversely, if the threshold was met or exceeded, then the fingers remained stationary and the gripper moved upward to lift the cup.

The robotic demonstration was performed using the multimodal 3D sensor array both with and without calibrated compensation. Initially, the 3D sensor array, when operated without compensation, functioned solely as a pressure sensor. During this operation, real-time I_P data were converted to pressure values and plotted over time (Fig. 5C). In this uncompensated scenario, the gripper ceased movement when the pressure exceeded the threshold at $t = 48.4$ s but failed to lift the hot cup due to insufficient grasping force, a consequence of temperature-induced mismeasurements (Fig. 5D). Conversely, with the calibrated compensation activated, the gripper adjusted its grasp, moving closer to the cup, reaching the pressure threshold at $t = 57.2$ s (Fig. 5C). The adjustment was enabled by compensation that corrected for mismeasurements by thermal effects, allowing precise control until the accurate pressure was detected. The real-time spatiotemporal pressure and temperature data, captured during the compensated operation, showed initial readings at 31°C with negligible pressure, increasing to 45°C as the gripper approached the hot cup (Fig. 5, F and G). The compensated sensor maintained pressure below the threshold until reaching it after $t = 48.4$ s, contrary to the demonstration without compensation. After two more movements ($t = 57.2$ s), the gripper eventually stopped when the threshold was reached. Then, it successfully lifted the hot cup (Fig. 5E). The robotic demonstration was recorded in real time (movie S2). The result showed that the developed 3D sensor array could detect real-time 2D distributions of temperature and pressure without cross-sensitivity, which successfully enabled the robotic gripper to lift objects regardless of temperature. Moreover, the multimodal sensor provided consistent, temperature-independent pressure data even as the cup's temperature changed in real time (fig. S11). After achieving a stable grip, the cup was heated on a hotplate, gradually reaching a temperature of 50°C over a duration of 6 min. The multimodal sensor collected I_{T*}, uncompensated I_P, and temperature-compensated I_P data in real time. Without compensation, the I_P values increased as the cup's temperature rose due to thermal distortion of the pressure sensor. In contrast, the compensated I_P data consistently maintained a stable pressure level, as thermal effects were calibrated in real time. Consequently, the gripper was able to hold the cup stably, demonstrating the smart gripper's capability to operate efficiently under varying temperature conditions.

Downloaded from https://www.science.org at Ulsan National Institute of Science and Technology on February 04, 2025

DISCUSSION

This study presents a multimodal sensor array using the 3D transistor-on-transistor active-matrix design for precise spatial measurement of pressure and temperature, demonstrating exceptional stimulus discriminability. Each sensor pixel, comprising monolithically stacked 3D TFTs integrated with a high-sensitivity piezoresistive sheet, exhibited reliable performance. Our sensor array facilitated simultaneous detection of temperature and pressure in a single spot. To address the unwanted thermal effect on pressure readings, we developed a calibrated compensation method, leveraging the linear and consistent temperature sensitivity. This compensation process significantly mitigated temperature-induced inaccuracies, allowing the sensor array to measure spatial distributions of pressure and temperature without signal distortion. The practical application of this technology was exemplified through a robotic gripper demonstration, demonstrating the ability to grasp and lift objects irrespective of their temperature variations.

The 3D sensor-on-sensor architecture proposed here offers a promising advancement for TFT-based sensors, traditionally susceptible to temperature changes. Although TFT platforms are optimal for 2D spatial signal mapping due to their high accuracy and minimal cross-talk (*53*), they remain sensitive to thermal variations—a challenge stemming from the inherent temperature dependency of charge transport in semiconductors. This work not only addresses these challenges through innovative 3D integration, allowing simultaneous temperature compensation at the sensor site, but also proposes a universal solution for reducing cross-sensitivity in active-matrix sensors, independent of material or sensing mechanism specifics. This strategy would herald a new era in electronics that mimic real skin, capable of sensing and interacting with a multitude of physical signals, marking a notable stride toward next-generation sensor technology.

MATERIALS AND METHODS

Material preparation

A silver nanoparticle ink (NPS-L, Harimatec Inc.) was used as a conductive ink for all electrodes and interconnects in this work. The work function of the silver contact electrodes was modified by self-assembled monolayers of a 30 mM 2,3,4,5,6-pentafluorothiophenol (PFBT) (Sigma-Aldrich) solution dissolved in isopropanol. For the p-type semiconductor ink, DPP-DTT (M0311A, Ossila) was prepared in 2 mg/ml using chlorobenzene (Sigma-Aldrich). A hydrophobic polymer (Teflon AF1600, Dupont) ink was prepared in a 1 weight % (wt %) solution using perfluorotributylamine (Fluorinert FC-43, 3 M) and used to define the area to be filled with the semiconductor. All inks were filtered with polytetrafluoroethylene membrane filters with a 0.45-μm pore size. A fluoropolymer CYTOP (CTL-809 M, AGC) was dissolved in CT-SOLV180 (AGC) with a volume ratio of 1:4 and used to deposit a solution-processed dielectric layer. A poly(p-xylylene) derivative (Parylene diX-SR, KISCO Ltd.) was used to deposit the conformal dielectric layers. A PVDF (molecular weight: ~534,000, Sigma-Aldrich) was prepared in a 20 wt % dispersion using dimethylformamide (DMF). A 1.05 wt % GO-DMF dispersion was prepared by the modified Hummers methods (*54*). The PVDF dispersion and GO dispersion were mixed at desired mixing ratio. A microdome array replica mold was prepared using a microdome-patterned silicon master mold with a 10-μm diameter, 12-μm pitch, and 4-μm height.

Device fabrication

A glass substrate (Eagle XG, Corning) was coated with surfactant and 3-μm–thick parylene (KISCO Ltd.), which can be peeled off as needed. On the parylene surface, bottom S/D electrodes were inkjet-printed using a drop-on-demand inkjet printer (DMP 2850, Fujifilm Dimatix) and sintered at 120°C for 1 hour. The contact electrodes in each row were connected to realize an active matrix. To define the semiconductor area, the Teflon ink was printed using a dispensing machine (350PC, MUSASHI ENGINEERING Inc.) and annealed at 100°C for 10 min. Then, the S/D electrodes were dipped into a PFBT solution for 5 min and rinsed. The semiconductor ink was dispensed to fill the area defined by Teflon and annealed at 100°C for 30 min. The Teflon pattern was removed by immersion in perfluorotributylamine. A CYTOP dielectric film with a thickness of 50 nm was deposited by spin coating. Next, a 200-nm–thick parylene gate dielectric was deposited. The bottom active-matrix fabrication was finished by inkjet-printing vertically shared gate electrodes. The gate electrodes in each column were connected to realize an active matrix. On the gate electrodes, a 200-nm–thick gate dielectric was deposited. Top S/D electrodes were inkjet-printed on the gate dielectric. After sintering, only source electrodes in each row were connected to realize an active matrix. Again, Teflon patterns, a PFBT layer, DPP-DTT patterns, a 50-nm–thick CYTOP dielectric, and a 200-nm–thick parylene passivation layer were formed in sequence. Laser-drilled via-holes were formed on the top drain electrodes and filled with inkjet-printed contact pads exposed to air. The piezoresistive sheets were fabricated separately. A PVDF-GO-DMF dispersion was poured onto the replica mold and dried at 50°C for 12 hours. The dried GO/PVDF microdome-patterned film was annealed at 160°C for 2 hours. The annealing process led to the formation of reduced GO (rGO) and the removal of residual solvent. To realize an interlocked microdome structure, two rGO/PVDF composite films were faced each other with an inserted 10-μm-thick plastic spacer. The spacer was attached to the composite films at the edge of the films. After the attachment, the top layer was spay-coated with silver nanowires and used as an electrode. Last, the bottom layer of the piezoresistive sheet was attached to the contact pads of the stacked active matrix, and the top electrode of the sheet was connected to the ground nodes of the stacked device.

Electrical characterization

The sensing capabilities were characterized in an environment where temperature and pressure could vary. The temperature was controlled by a hotplate (SD160, Stuart), where the devices were placed. The pressure load was controlled by a force gauge (DS2-110, IMADA Inc.) mounted on a motorized *z*-axis linear stage with customized LabVIEW software (National Instruments Corp.). The transfer characteristics were measured using a semiconductor characterization system (4200A-SCS, Keithley). The 2D mapping was enabled by a custom-built array measurement system, which consisted of a PXI system (PXIe-8840, 4135, and 1076, National Instruments Corp.), a switch matrix system (E5250A and E5252A, Keysight), and a measurement jig with an adapter module. For the transfer characteristics measurement, the gate voltage was swept from 2 to −10 V, while the drain voltage remained fixed at −10 V. In all other experiments, the gate and drain voltages were fixed at −10 V.

Robotic demonstration

A commercially available robotic gripper (RM-X52-TNM, ROBOTIS) was used for the robotic demonstration. The gripper was controlled

Downloaded from https://www.science.org at Ulsan National Institute of Science and Technology on February 04, 2025

by customized LabVIEW software. The gripper control and measurement software were integrated into a single LabVIEW software.

Supplementary Materials

The PDF file includes:
Figs. S1 to S11
Legends for movies S1 and S2

Other Supplementary Material for this manuscript includes the following:
Movies S1 and S2

REFERENCES AND NOTES

1. S. Earley, L. F. Santana, W. J. Lederer, The physiological sensor channels TRP and piezo: Nobel Prize in Physiology or Medicine 2021. *Physiol. Rev.* **102**, 1153–1158 (2022).
2. H. U. Chung, B. H. Kim, J. Y. Lee, J. Lee, Z. Xie, E. M. Ibler, K. Lee, A. Banks, J. Y. Jeong, J. Kim, C. Ogle, D. Grande, Y. Yu, H. Jang, P. Assem, D. Ryu, J. W. Kwak, M. Namkoong, J. Bin Park, Y. Lee, D. H. Kim, A. Ryu, J. Jeong, K. You, B. Ji, Z. Liu, Q. Huo, X. Feng, Y. Deng, Y. Xu, K.-I. Jang, J. Kim, Y. Zhang, R. Ghaffari, C. M. Rand, M. Schau, A. Hamvas, D. E. Weese-Mayer, Y. Huang, S. M. Lee, C. H. Lee, N. R. Shanbhag, A. S. Paller, S. Xu, J. A. Rogers, Binodal, wireless epidermal electronic systems with in-sensor analytics for neonatal intensive care. *Science* **363**, eaau0780 (2019).
3. M. Han, L. Chen, K. Aras, C. Liang, X. Chen, H. Zhao, K. Li, N. R. Faye, B. Sun, J.-H. Kim, W. Bai, Q. Yang, Y. Ma, W. Lu, E. Song, J. M. Baek, Y. Lee, C. Liu, J. B. Model, G. Yang, R. Ghaffari, Y. Huang, I. R. Efimov, J. A. Rogers, Catheter-integrated soft multilayer electronic arrays for multiplexed sensing and actuation during cardiac surgery. *Nat. Biomed. Eng.* **4**, 997–1009 (2020).
4. Y. Lee, A. Carnicer-Lombarte, S. Han, B. J. Woodington, S. Chai, A. G. Polyravas, S. Velasco-Bosom, E.-H. Kim, G. G. Malliaras, S. Jung, Tunable organic active neural probe enabling near-sensor signal processing. *Adv. Mater.* **35**, e2301782 (2023).
5. S. Baek, H. Matsui, T. Mano, J. A. Park, Y. Jo, Y. Lee, S. Tokito, J. Kwon, S. Jung, Dual-gate thin film transistor lactate sensors operating in the subthreshold regime. *Biosens. Bioelectron.* **222**, 114958 (2023).
6. L. E. Osborn, A. Dragomir, J. L. Betthauser, C. L. Hunt, H. H. Nguyen, R. R. Kaliki, N. V. Thakor, Prosthesis with neuromorphic multilayered e-dermis perceives touch and pain. *Sci. Robot.* **3**, eaat3818 (2018).
7. J. Shin, B. Jeong, J. Kim, V. B. Nam, Y. Yoon, J. Jung, S. Hong, H. Lee, H. Eom, J. Yeo, J. Choi, D. Lee, S. H. Ko, Sensitive wearable temperature sensor with seamless monolithic integration. *Adv. Mater.* **32**, e1905527 (2020).
8. Q. Su, Q. Zou, Y. Li, Y. Chen, S.-Y. Teng, J. T. Kelleher, R. Nith, P. Cheng, N. Li, W. Liu, S. Dai, Y. Liu, A. Mazursky, J. Xu, L. Jin, P. Lopes, S. Wang, A stretchable and strain-unperturbed pressure sensor for motion interference–free tactile monitoring on skins. *Sci. Adv.* **7**, eabi4563 (2021).
9. Y. Zhang, J. Yang, X. Hou, G. Li, L. Wang, N. Bai, M. Cai, L. Zhao, Y. Wang, J. Zhang, K. Chen, X. Wu, C. Yang, Y. Dai, Z. Zhang, C. F. Guo, Highly stable flexible pressure sensors with a quasi-homogeneous composition and interlinked interfaces. *Nat. Commun.* **13**, 1317 (2022).
10. H. Liu, K. Sun, X.-L. Guo, Z.-L. Liu, Y.-H. Wang, Y. Yang, D. Yu, Y.-T. Li, T.-L. Ren, An ultrahigh linear sensitive temperature sensor based on PANI:Graphene and PDMS hybrid with negative temperature compensation. *ACS Nano* **16**, 21527–21535 (2022).
11. S. M. Won, H. Wang, B. H. Kim, K. Lee, H. Jang, K. Kwon, M. Han, K. E. Crawford, H. Li, Y. Lee, X. Yuan, S. B. Kim, Y. S. Oh, W. J. Jang, J. Y. Lee, S. Han, J. Kim, X. Wang, Z. Xie, Y. Zhang, Y. Huang, J. A. Rogers, Multimodal sensing with a three-dimensional piezoresistive structure. *ACS Nano* **13**, 10972–10979 (2019).
12. M. Liu, Y. Zhang, J. Wang, N. Qin, H. Yang, K. Sun, J. Hao, L. Shu, J. Liu, Q. Chen, P. Zhang, T. H. Tao, A star-nose-like tactile-olfactory bionic sensing array for robust object recognition in non-visual environments. *Nat. Commun.* **13**, 79 (2022).
13. Y. Yu, J. Li, S. A. Solomon, J. Min, J. Tu, W. Guo, C. Xu, Y. Song, W. Gao, All-printed soft human-machine interface for robotic physicochemical sensing. *Sci. Robot.* **7**, eabn0495 (2022).
14. P. Zhu, Y. Wang, Y. Wang, H. Mao, Q. Zhang, Y. Deng, Flexible 3D architectured piezo/thermoelectric bimodal tactile sensor array for e-skin application. *Adv. Energy Mater.* **10**, 2001945 (2020).
15. J. H. Lee, J. S. Heo, Y.-J. Kim, J. Eom, H. J. Jung, J.-W. Kim, I. Kim, H.-H. Park, H. S. Mo, Y.-H. Kim, S. K. Park, A behavior-learned cross-reactive sensor matrix for intelligent skin perception. *Adv. Mater.* **32**, e2000969 (2020).
16. R. Yang, W. Zhang, N. Tiwari, H. Yan, T. Li, H. Cheng, Multimodal sensors with decoupled sensing mechanisms. *Adv. Sci.* **9**, e2202470 (2022).
17. J. Park, M. Kim, Y. Lee, H. S. Lee, H. Ko, Fingertip skin–inspired microstructured ferroelectric skins discriminate static/dynamic pressure and temperature stimuli. *Sci. Adv.* **1**, e1500661 (2015).
18. S. Zhao, R. Zhu, Electronic skin with multifunction sensors based on thermosensation. *Adv. Mater.* **29**, 1606151 (2017).
19. Q. Hua, J. Sun, H. Liu, R. Bao, R. Yu, J. Zhai, C. Pan, Z. L. Wang, Skin-inspired highly stretchable and conformable matrix networks for multifunctional sensing. *Nat. Commun.* **9**, 244 (2018).
20. I. You, D. G. Mackanic, N. Matsuhisa, J. Kang, J. Kwon, L. Beker, J. Mun, W. Suh, T. Y. Kim, J. B.-H. Tok, Z. Bao, U. Jeong, Artificial multimodal receptors based on ion relaxation dynamics. *Science* **370**, 961–965 (2020).
21. M. Cai, Z. Jiao, S. Nie, C. Wang, J. Zou, J. Song, A multifunctional electronic skin based on patterned metal films for tactile sensing with a broad linear response range. *Sci. Adv.* **7**, eabl8313 (2021).
22. X. Fu, Z. Zhuang, Y. Zhao, B. Liu, Y. Liao, Z. Yu, P. Yang, K. Liu, Stretchable and self-powered temperature–Pressure dual sensing ionic skins based on thermogalvanic hydrogels. *ACS Appl. Mater. Interfaces* **14**, 44792–44798 (2022).
23. Y.-E. Shin, Y.-J. Park, S. K. Ghosh, Y. Lee, J. Park, H. Ko, Ultrasensitive multimodal tactile sensors with skin-inspired microstructures through localized ferroelectric polarization. *Adv. Sci.* **9**, e2105423 (2022).
24. H. Zhang, H. Chen, J.-H. Lee, E. Kim, K.-Y. Chan, H. Venkatesan, M. H. Adegun, O. G. Agbabiaka, X. Shen, Q. Zheng, J. Yang, J.-K. Kim, Bioinspired chromotropic ionic skin with in-plane strain/temperature/pressure multimodal sensing and ultrahigh stimuli discriminability. *Adv. Funct. Mater.* **32**, 2208362 (2022).
25. H. Shim, K. Sim, F. Ershad, S. Jang, C. Yu, Recent advances in materials and device technologies for soft active matrix electronics. *J. Mater. Chem. C* **8**, 10719–10731 (2020).
26. S. Baek, G. Y. Bae, J. Kwon, K. Cho, S. Jung, Flexible pressure-sensitive contact transistors operating in the subthreshold regime. *ACS Appl. Mater. Interfaces* **11**, 31111–31118 (2019).
27. K. Sim, F. Ershad, Y. Zhang, P. Yang, H. Shim, Z. Rao, Y. Lu, A. Thukral, A. Elgalad, Y. Xi, B. Tian, D. A. Taylor, C. Yu, An epicardial bioelectronic patch made from soft rubbery materials and capable of spatiotemporal mapping of electrophysiological activity. *Nat. Electron.* **3**, 775–784 (2020).
28. S. Hong, N. Zagni, S. Choo, N. Liu, S. Baek, A. Bala, H. Yoo, B. H. Kang, H. J. Kim, H. J. Yun, M. A. Alam, S. Kim, Highly sensitive active pixel image sensor array driven by large-area bilayer MoS_2 transistor circuitry. *Nat. Commun.* **12**, 3559 (2021).
29. C. Becker, B. Bao, D. D. Karnaushenko, V. K. Bandari, B. Rivkin, Z. Li, M. Faghih, D. Karnaushenko, O. G. Schmidt, A new dimension for magnetosensitive e-skins: Active matrix integrated micro-origami sensor arrays. *Nat. Commun.* **13**, 2121 (2022).
30. L. A. Ruiz-Preciado, S. Baek, N. Strobel, K. Xia, M. Seiberlich, S.-m. Park, U. Lemmer, S. Jung, G. Hernandez-Sosa, Monolithically printed all-organic flexible photosensor active matrix. *npj Flex. Electron.* **7**, 6 (2023).
31. R. Kawabata, K. Li, T. Araki, M. Akiyama, K. Sugimachi, N. Matsuoka, N. Takahashi, D. Sakai, Y. Matsuzaki, R. Koshimizu, M. Yamamoto, L. Takai, R. Odawara, T. Abe, S. Izumi, N. Kurihira, T. Uemura, Y. Kawano, T. Sekitani, Ultraflexible wireless imager integrated with organic circuits for broadband infrared thermal analysis. *Adv. Mater.* **36**, 2309864 (2024).
32. J. S. Kim, M. W. Jeong, T. U. Nam, N. T. P. Vo, K. H. Jung, T. Il Lee, J. Y. Oh, Intrinsically stretchable subthreshold organic transistors for highly sensitive low-power skin-like active-matrix temperature sensors. *Adv. Funct. Mater.* **34**, 2305252 (2024).
33. T. Someya, T. Sekitani, S. Iba, Y. Kato, H. Kawaguchi, T. Sakurai, A large-area, flexible pressure sensor matrix with organic field-effect transistors for artificial skin applications. *Proc. Natl. Acad. Sci. U.S.A.* **101**, 9966–9970 (2004).
34. T. Sakanoue, H. Sirringhaus, Band-like temperature dependence of mobility in a solution-processed organic semiconductor. *Nat. Mater.* **9**, 736–740 (2010).
35. C. Chen, K. Abe, H. Kumomi, J. Kanicki, Density of states of a-InGaZnO from temperature-dependent field-effect studies. *IEEE Trans. Electron Devices* **56**, 1177–1183 (2009).
36. S. Zhou, G. Zhou, Y. Li, X. Xu, Y. J. Hsu, J. Xu, N. Zhao, X. Lu, Understanding charge transport in all-inorganic halide perovskite nanocrystal thin-film field effect transistors. *ACS Energy Lett.* **5**, 2614–2623 (2020).
37. B. Radisavljevic, A. Kis, Mobility engineering and a metal-insulator transition in monolayer MoS_2. *Nat. Mater.* **12**, 815–820 (2013).
38. T. Someya, Y. Kato, T. Sekitani, S. Iba, Y. Noguchi, Y. Murase, H. Kawaguchi, T. Sakurai, Conformable, flexible, large-area networks of pressure and thermal sensors with organic transistor active matrixes. *Proc. Natl. Acad. Sci. U.S.A.* **102**, 12321–12325 (2005).
39. J. Zhao, Z. Wei, Z. Li, J. Yu, J. Tang, G. Zhang, Z. Wang, Skin-inspired high-performance active-matrix circuitry for multimodal user-interaction. *Adv. Funct. Mater.* **31**, 2105480 (2021).
40. J. Park, J. Kim, J. Hong, H. Lee, Y. Lee, S. Cho, S. W. Kim, J. J. Kim, S. Y. Kim, H. Ko, Tailoring force sensitivity and selectivity by microstructure engineering of multidirectional electronic skins. *NPG Asia Mater.* **10**, 163–176 (2018).
41. S. Baek, Y. Lee, J. Baek, J. Kwon, S. Kim, S. Lee, K.-P. Strunk, S. Stehlin, C. Melzer, S.-M. Park, H. Ko, S. Jung, Spatiotemporal measurement of arterial pulse waves enabled by wearable active-matrix pressure sensor arrays. *ACS Nano* **16**, 368–377 (2022).
42. P. Wei, Z. Shen, X. Qin, P. Zhang, L. Bu, Q. Chen, S. V. Roth, G. Lu, Improving charge injection at gold/conjugated polymer contacts by polymer insulator-assisted annealing for transistors. *Small* **18**, e2105896 (2022).

Downloaded from https://www.science.org at Ulsan National Institute of Science and Technology on February 04, 2025

43. Y. Lee, J. Myoung, S. Cho, J. Park, J. Kim, H. Lee, Y. Lee, S. Lee, C. Baig, H. Ko, Bioinspired gradient conductivity and stiffness for ultrasensitive electronic skins. *ACS Nano* **15**, 1795–1804 (2021).
44. G. Havenith, E. J. G. van de Linde, R. Heus, Pain, thermal sensation and cooling rates of hands while touching cold materials. *Eur. J. Appl. Physiol. Occup. Physiol.* **65**, 43–51 (1992).
45. R. Defrin, M. Shachal-Shiffer, M. Hadgadg, C. Peretz, Quantitative somatosensory testing of warm and heat-pain thresholds: The effect of body region and testing method. *Clin. J. Pain* **22**, 130–136 (2006).
46. J.-F. Chang, H. Sirringhaus, M. Giles, M. Heeney, I. McCulloch, Relative importance of polaron activation and disorder on charge transport in high-mobility conjugated polymer field-effect transistors. *Phys. Rev. B* **76**, 205204 (2007).
47. R. Nirosha, R. Agarwal, Comprehensive temperature-dependent DC characterization of organic thin film transistor for sensing applications. *IEEE Sens. J.* **22**, 16794–16803 (2022).
48. S. Y. Hong, Y. H. Lee, H. Park, S. W. Jin, Y. R. Jeong, J. Yun, I. You, G. Zi, J. S. Ha, Stretchable active matrix temperature sensor array of polyaniline nanofibers for electronic skin. *Adv. Mater.* **28**, 930–935 (2016).
49. X. Ren, K. Pei, B. Peng, Z. Zhang, Z. Wang, X. Wang, P. K. L. Chan, A low-operating-power and flexible active-matrix organic-transistor temperature-sensor array. *Adv. Mater.* **28**, 4832–4838 (2016).
50. Y.-F. Wang, T. Sekine, Y. Takeda, K. Yokosawa, H. Matsui, D. Kumaki, T. Shiba, T. Nishikawa, S. Tokito, Fully printed PEDOT:PSS-based temperature sensor with high humidity stability for wireless healthcare monitoring. *Sci. Rep.* **10**, 2467 (2020).
51. A. Daus, M. Jaikissoon, A. I. Khan, A. Kumar, R. W. Grady, K. C. Saraswat, E. Pop, Fast-response flexible temperature sensors with atomically thin molybdenum disulfide. *Nano Lett.* **22**, 6135–6140 (2022).
52. Y. Qiu, Z. Wang, P. Zhu, B. Su, C. Wei, Y. Tian, Z. Zhang, H. Chai, A. Liu, L. Liang, H. Wu, A multisensory-feedback tactile glove with dense coverage of sensing arrays for object recognition. *Chem. Eng. J.* **455**, 140890 (2023).
53. Y. J. Park, B. K. Sharma, S. M. Shinde, M.-S. Kim, B. Jang, J.-H. Kim, J.-H. Ahn, All MoS_2-based large area, skin-attachable active-matrix tactile sensor. *ACS Nano* **13**, 3023–3030 (2019).
54. W. S. Hummers Jr., R. E. Offeman, Preparation of graphitic oxide. *J. Am. Chem. Soc.* **80**, 1339 (1958).

Acknowledgments

Funding: This work was supported by the National Research Foundation of Korea (NRF) grants (NRF-2022R1A2C2012272 and RS-2024-00403376) funded by the Korea government (MSIT).

Author contributions: Conceptualization: Y.J., S.B., H.K., and S.J. Methodology: Y.J., Y.L., S.B., H.K., and S.J. Software: Y.J. and S.K. Validation: Y.J., Y.L., and S.B. Formal analysis: Y.J. and S.B. Investigation: Y.J., Y.L., G.R., S.Y., S.B., and S.J. Resources: S.B., H.K., and S.J. Data curation: Y.J., Y.L., J.K., S.K., S.B., H.K., and S.J. Writing—original draft: Y.J., J.K., S.B., H.K., and S.J. Writing—review and editing: Y.J., J.K., S.B., H.K., and S.J. Visualization: Y.J., J.K., G.R., S.Y., S.B., H.K., and S.J. Supervision: H.K. and S.J. Project administration: S.B., H.K., and S.J. Funding acquisition: S.J.
Competing interests: Y.J., S.B., and S.J. are authors on a patent application (US20240337544A1 published on 10 October 2024) related to this work filed by Postech Research and Business Development Foundation. The other authors declare that they have no other competing interests. **Data and materials availability:** All data needed to evaluate the conclusions in the paper are present in the paper and/or the Supplementary Materials.

Submitted 16 August 2024
Accepted 17 December 2024
Published 17 January 2025
10.1126/sciadv.ads4516

Downloaded from https://www.science.org at Ulsan National Institute of Science and Technology on February 04, 2025